Spatially isotropic four-dimensional imaging with dual-view plane illumination microscopy

Yicong Wu[1], **Peter Wawrzusin**[1], **Justin Senseney**[2], **Robert S Fischer**[3], **Ryan Christensen**[4,5], **Anthony Santella**[6], **Andrew G York**[1], **Peter W Winter**[1], **Clare M Waterman**[3], **Zhirong Bao**[6], **Daniel A Colón-Ramos**[4,5], **Matthew McAuliffe**[2], and **Hari Shroff**[1]

[1]Section on High Resolution Optical Imaging, National Institute of Biomedical Imaging and Bioengineering, National Institutes of Health, Bethesda, Maryland, USA

[2]Biomedical Imaging Research Services Section, Center for Information Technology, National Institutes of Health, Bethesda, Maryland, USA

[3]National Heart, Lung, and Blood Institute, National Institutes of Health, Bethesda, Maryland, USA

[4]Program in Cellular Neuroscience, Neurodegeneration and Repair, Yale University School of Medicine, New Haven, Connecticut, USA

[5]Department of Cell Biology, Yale University School of Medicine, New Haven, Connecticut, USA

[6]Developmental Biology Program, Sloan-Kettering Institute, New York, New York, USA

Abstract

Optimal four-dimensional imaging requires high spatial resolution in all dimensions, high speed and minimal photobleaching and damage. We developed a dual-view, plane illumination microscope with improved spatiotemporal resolution by switching illumination and detection between two perpendicular objectives in an alternating duty cycle. Computationally fusing the resulting volumetric views provides an isotropic resolution of 330 nm. As the sample is stationary and only two views are required, we achieve an imaging speed of 200 images/s (i.e., 0.5 s for a 50-plane volume). Unlike spinning-disk confocal or Bessel beam methods, which illuminate the sample outside the focal plane, we maintain high spatiotemporal resolution over hundreds of volumes with negligible photobleaching. To illustrate the ability of our method to study biological systems that require high-speed volumetric visualization and/or low photobleaching, we describe

microtubule tracking in live cells, nuclear imaging over 14 h during nematode embryogenesis and imaging of neural wiring during *Caenorhabditis elegans* brain development over 5 h.

Combining genetically expressed markers with fluorescence microscopy enables interrogation of live samples with high contrast and specificity but is of limited utility unless imaging is performed noninvasively. When interrogating three-dimensional samples over time (four dimensional, or 4D, imaging), optimal imaging also demands the rejection of out-of-focus light (optical sectioning). Light sheet–based fluorescence microscopy (LSFM[1-4]) satisfies these requirements, affording major advantages over other 4D imaging tools such as confocal laser scanning microscopy (CLSM) or spinning-disk confocal microscopy (SDCM): (i) excitation is parallelized to the extent that fluorophore saturation is minimized and a high signal-to-noise ratio can be maintained at high frame rates; (ii) limiting the sheet illumination to the vicinity of the focal plane minimizes photobleaching and photodamage. These advantages result in an imaging system well-suited for 4D studies of developmental biology[5], yet widespread adoption of LSFM by biologists has been slow owing to its cumbersome design and poor axial resolution.

Most LSFM implementations are built around the specimen, embedding the sample in agarose, thereby precluding conventional sample mounts such as glass coverslips. Even if the versatility of LSFM is improved by implementing it on a conventional microscope base (e.g., inverted selective plane illumination microscopy, iSPIM[6,7]), the requisite orthogonality between excitation and detection axes prevents the use of the highest available numerical aperture (NA) detection objectives, so axial resolution is usually several micrometers (or worse). If the light sheet is made sufficiently thin, axial resolution can be decoupled from detection NA, enabling more isotropic resolution. As most light sheets use Gaussian beams, they undergo diffractive spreading at distances far from the beam waist and thicken significantly unless a relatively large beam waist is chosen. Synthesizing light sheets from Bessel beams[8] circumvents this problem[9], but introduces extraneous illumination outside the focal plane, subjecting the sample to much more photobleaching and photodamage than standard LSFM.

An alternative method that improves resolution isotropy relies on computationally fusing multiple specimen views (6–36 views) taken at different detection angles[10,11]. Although this technique results in improved axial resolution, the fusion procedure also reduces lateral resolution unless many volumetric views are acquired. Each additional view results in an increased dose to the sample, offsetting the original advantage of LSFM. Furthermore, because such acquisitions are usually implemented by rotating the specimen while maintaining a single illumination and detection path[10,12], they are too slow for visualizing many biological dynamics, such as fast nuclear movements[13,14].

Thus, previous attempts to improve axial resolution compromise imaging speed, increase excitation dose and photobleach the sample substantially more than single-view LSFM microscopes with anisotropic resolution. By simply alternating excitation and detection between two perpendicular objectives and combining the resulting views appropriately, we have developed a solution that enables isotropic imaging without mitigating the original advantages of light sheet microscopy. The resulting system enables sustained volumetric

imaging at rates 10–1,000× faster than have been reported for other 4D microscopy techniques.

RESULTS

Improving resolution isotropy with a second specimen view

Any conventional lens collects fewer spatial frequencies along its detection axis than perpendicular to it, resulting in two- to threefold poorer axial than lateral resolution in most single-view microscopes. We hypothesized that we could improve the resolution of our iSPIM setup[6,7] if a complementary, perpendicular view were also acquired and properly merged with the conventional iSPIM view, as the additional information would improve axial resolution without compromising lateral resolution. Thus, we developed a symmetrical dual-view iSPIM (diSPIM) to obtain two perpendicular views of the specimen, using two identical 0.8 NA objectives (the highest NA option that is commercially available given the requirement that both objectives fit in our setup) for sequential excitation and detection along each arm of the microscope (Fig. 1 and Supplementary Fig. 1).

Point spread function (PSF) measurements using 100-nm fluorescent beads revealed the expected anisotropic resolution inherent in either view (lateral FWHM: 0.47 ± 0.02 μm; axial FWHM: 1.47 ± 0.19 μm, $N = 10$ beads across our imaging field of ~30 μm; Fig. 2a and Supplementary Table 1). Deconvolving either view improved both lateral and axial resolution, but still resulted in an anisotropic PSF (Fig. 2b). Previous attempts to improve resolution by combining multiple views[15] relied on arithmetic fusion. We thus attempted to increase resolution isotropy by rotating, registering and fusing view$_B$ to view$_A$ (Supplementary Fig. 2). Although arithmetic fusion (Fig. 2c) improved the axial FWHM, equally weighting both views introduced 'wings' into the PSF because of the lower axial spatial frequencies present in each view. Lateral resolution was thus compromised as a result. Deconvolving each view before fusion improved resolution isotropy (Fig. 2d), but still resulted in a slightly anisotropic PSF that had lower lateral resolution than either single view after deconvolution (Fig. 2b).

We reasoned that a joint deconvolution scheme that made the best use of the information present in each view would provide results superior to those of simple arithmetic fusion of both views or deconvolution of either view alone. Joint deconvolution based on least-squares minimization has previously been shown to improve resolution isotropy[12], but requires 6–36 views of the sample and 15- to 30-min volumetric acquisition times due to the need for sample rotation. The recent use of ultrafast rotation stages in light sheet microscopy may provide a much faster implementation of multiview SPIM[16], yet such an approach still requires physical rotation of the sample and may thus introduce undesirable accelerations in some samples. Here, we designed a method that isotropizes resolution with only two perpendicular views of the sample, which are sequentially acquired without moving the sample.

Iterative Richardson-Lucy deconvolution[17,18] improves an estimate of the sample by changing the estimate everywhere it disagrees with the measurement and is commonly used

to improve single-view data corrupted by Poisson noise[19]. For a symmetrical PSF, the iteration loop may be summarized as

$$For\ i=1,2,\ldots.N\ (i.e., iteration\ number)$$
$$New\_\ estimate=Previous\_\ estimate \times Blur\left(\frac{Measured\_\ image}{Blur(Previous\_\ estimate)}\right)$$
$$End$$

where Blur() indicates convolution with the PSF.

Because any single view has an anisotropic PSF, even after this procedure, the resulting estimate is badly blurred in the axial direction. However, diSPIM acquires two measurements of the same object from perpendicular views. By modifying the Richardson-Lucy algorithm to provide an estimate that is consistent with both complementary measurements, we removed the axial ambiguity, effectively preserving the best (lateral) resolution in each view and replacing its poor (axial) resolution with the best (lateral) resolution inherent to the other view

$$Estimate_0=(View_A+View_B)/2$$
$$For\ i=1,2,\ldots.N\ (i.e., iteration\ number)$$
$$Estimate_A=Estimate_{i-1} \times Blur_A\left(\frac{View_A}{Blur_A\ (Estimate_{i-1})}\right)$$
$$Estimate_i=Estimate_A \times Blur_B\left(\frac{View_B}{Blur_B\ (Estimate_A)}\right)$$
$$End$$

where $Estimate_0$ is the initial estimate provided by the average of the dual volumetric views $view_A$ and $View_B$, $Blur_A$ corresponds to convolution with the PSF associated with the volumetric $view_A$ and $Blur_B$ corresponds to convolution with the PSF associated with volumetric $View_B$.

Using the two diSPIM views in our joint deconvolution method resulted in an isotropic resolution of 330 nm, more than quadrupling axial resolution and improving lateral resolution ~1.4× over either single raw view (Fig. 2e,f, Supplementary Table 1 and Supplementary Video 1). This resolution was equivalent to the lateral resolution present in either view after deconvolution (Fig. 2b), suggesting that the algorithm advantageously recovered the highest spatial frequencies present in either view without introducing wings in the PSF.

We found that the majority of the resolution improvement occurs in ~10 iterations (used for the remaining data presented in this paper), whereas convergence is reached in ~30 iterations requiring 20 s/volume on a six-core computer. Although others have proposed and implemented a similar (but not identical) multiview deconvolution algorithm[11,20], we found that our algorithm converged faster (Supplementary Fig. 3 and Supplementary Note 1). Given the large volume of data in some LSFM applications, this may prove a significant advantage.

Our algorithm provides isotropic resolution even when using widefield, not planar, illumination (Supplementary Fig. 4). Although widefield illumination is undesirable when

imaging thick threedimensional (3D) specimens because of the greater bleaching, photodamage and background it causes, this result suggests that our method retains its performance even over larger imaging fields than we tested, at distances further from the sheet waist.

Extending these results on stationary fluorescent beads to live 3D biological samples requires high temporal as well as spatial resolution. We therefore sought to acquire both sequential views rapidly, replacing the slower electron-multiplying, charge-coupled device camera used in previous experiments[6] with two scientific-grade, complementary, metal-oxide, semiconductor cameras. By synchronizing illumination with the rolling shutter detection cycle of the camera (Supplementary Figs. 5 and 6), we minimized readout noise (Supplementary Fig. 7), removed readout artifacts (Supplementary Fig. 8) and operated the cameras at high-frame rates (200 Hz using a 480×432 pixels field of view).

DiSPIM enables 3D microtubule tip tracking in live cells

The regulated self-assembly of microtubules is required for subcellular organization that promotes specialized cell functions in, for example, the nervous, vascular, immune and reproductive systems. Microtubules are 25 nm in diameter, and they assemble and disassemble on the timescale of seconds[21]. Because current 4D microscopy methods are plagued by anisotropic spatial resolution and poor time resolution, the mechanisms governing microtubule assembly have—to the best of our knowledge—never been probed in 3D *in vivo*, and studies have been limited to tissue culture model systems where microtubule dynamics are largely confined to two dimensions. Thus, the regulation of microtubule assembly in cellular function in important physiologically relevant tissues is largely unknown.

As an illustration that the speed and resolution of diSPIM is sufficient for studying microtubule assembly dynamics in 3D, we performed time-lapse imaging of whole cellular volumes of human umbilical vein endothelial cells on two-dimensional coverslips as well as in 3D collagen gels. We expressed the fluorescent tip-tracking protein GFP-EB3 that marks the growing plus ends of microtubules[22]. We compared diSPIM to the current state-of-the-art method, which rapidly acquires images in single focal planes over time by SDCM, followed by image analysis with semi-automated tip-tracking software to obtain rates of microtubule assembly[23]. SDCM is not ideal for 4D imaging of microtubule dynamics because (i) the poor axial resolution inhibits segmentation of growing ends in cell areas dense with microtubules; (ii) volumetric illumination induces rapid photobleaching in extended 3D time series; (iii) the integration time for images with high signal-to-noise ratios slows the acquisition rate for 3D volumes, leading to blurring and/or motion artifacts and calculation of unreliable microtubule assembly rates (Fig. 3a,b and Supplementary Video 2). By contrast, diSPIM allowed us to visualize 3D microtubule assembly dynamics with isotropic resolution, high temporal resolution (1 volume per second with a total volume size of ~40 μm × 40 μm × 20 μm), over extended time periods, and with negligible photobleaching (Fig. 3a,b and Supplementary Videos 2,3). At a similar illumination dose and initial signal-to-noise ratio, diSPIM had a bleaching rate ~7.6-fold lower than SDCM's,

despite 3× greater temporal sampling and 3.2-fold more imaging planes per volume (Fig. 3c).

Our results show that the organization and speed of microtubule assembly is dictated by 3D cell shape. In cells that were relatively flat and grown on coverslips, microtubule assembly was confined mostly to the plane of the cell (Fig. 4a,c). Significantly thicker (10–18 μm) cells grown on coverslips displayed a greater angular spread in microtubule assembly trajectories, although there was still a bias toward the coverslip. In contrast, cells embedded within thick (>15 μm) collagen gels displayed microtubule assembly with no apparent directional bias. Because of the shape variability of cells embedded in 3D collagen gels, we could further investigate whether local cell shape affects microtubule assembly rates (Fig. 4b). This showed that microtubule ends confined by thin cell shapes assembled more slowly than microtubules in thicker cells (Fig. 4c). If decreased assembly speed was simply due to physical obstruction of the cell boundary[24,25], one would expect the duration of microtubule assembly events in thin cells to be shorter than in thicker cells. However, we found no difference in assembly duration regardless of cell shape (Fig. 4c). Thus, 3D cell shape affects the organization and speed of microtubule assembly. We are unaware of other imaging techniques that enable visualization and quantification of microtubule assembly accurately in 3D. Our results suggest that diSPIM will allow exploration of the mechanisms governing microtubule dynamics in the vascular, nervous, immune and reproductive systems *in situ*.

Improved imaging of nuclear dynamics throughout embryogenesis

We next investigated the suitability of diSPIM for 4D imaging *in situ* in a developing animal by imaging embryogenesis in *C. elegans*. The invariant cell lineage of *C. elegans*[26] and its relative transparency make it a useful system for optically investigating development *in vivo*[6]. However, the larger size and correspondingly greater degree of scattering and depth-dependent aberrations[27] in nematode embryos make them more difficult to image than single cells. At the same time, embryogenesis is sensitive to cumulative phototoxicity, which has greatly limited the spatiotemporal resolution possible in long-term imaging of cellular organization and movement over the 14-h developmental period. In particular, imaging through the latter half of embryogenesis requires fast volumetric acquisition to minimize motion artifacts caused by muscular movements of the animal.

A unique feature of diSPIM is that data may be coarsely sampled (lower than the Nyquist sampling rate) in both axial directions without significantly degrading image quality or resolution (Supplementary Fig. 9). We took advantage of this feature when imaging nematode embryos, increasing speed (0.5 s for each dual-volume acquisition) and reducing phototoxicity with coarse axial spacing (1 μm) between acquisition planes in each volumetric view.

Compared to iSPIM, the added view in diSPIM improved axial resolution and reduced depth-dependent image deterioration without causing noticeable phototoxicity. Nematode strains carrying GFP-histone markers have been well-characterized by SDCM[28,29], allowing us to compare directly the performance of single- and dual-view iSPIM to this more commonly used technology (Fig. 5). We fixed the imaging frequency at 1 volume/min and

maintained a constant 1-μm interplane spacing in our comparisons between SDCM, iSPIM and diSPIM. These parameters ensured no abnormalities in the imaged embryos in terms of morphology or the timing and orientation of blastomere divisions, gastrulation, pharyngeal shape, elongation, twitching and hatching over the 14-h imaging period (Fig. 5a and Supplementary Videos 4,5). Compared to iSPIM and SDCM, the diSPIM data sets did not suffer axial distortion, minimized image degradation at the edges of the field and revealed subnuclear structure that was otherwise obscured by diffraction (Fig. 5b). We note that our voxel size of $0.1625 \times 0.1625 \times 0.1625$ μm^3 is 2–3× smaller than more invasive imaging methods such as CLSM or Bessel plane illumination when applied to nematode embryos[30], yet our imaging duration is ~1.5× longer.

DiSPIM also possessed sufficient acquisition speed to overcome the majority of motion blur caused by fast muscular twitching in the second half of embryogenesis (Supplementary Video 5). Such motion caused severe artifacts in the data sets collected using SDCM, eliminating it as a viable 4D imaging method in this period (Supplementary Video 4). With diSPIM, we observed an increase in noticeable blurring artifacts from ~2% (just after twitching) to ~25% (immediately preceding hatching) of all volumes, suggesting that twitching movements increased in speed over the course of embryogenesis (Supplementary Fig. 10). We were nevertheless still able to successfully register and jointly deconvolve most diSPIM volumes, obtaining improved resolution and contrast as in pre-twitching stages (Fig. 5a, Supplementary Fig. 11 and Supplementary Video 5). We are unaware of any other LSFM method capable of following nuclear movements in the post-twitching regime, as other methods with similar reported resolution are 10–1,000× slower[12,31].

Spatiotemporal dissection of neuronal outgrowths in live embryos

Although *C. elegans* is the only organism for which the wiring diagram of the complete nervous system is known[32], the process by which neurons dynamically establish wiring during development remains elusive. We had previously imaged neurite outgrowth in the pair of canal-associated neurons using iSPIM[6], but limitations in spatial resolution hindered our ability to visualize smaller neurites in additional neuron classes, particularly in the nerve ring region (equivalent to the nematode brain). DiSPIM allowed us to rotate volumes virtually without any loss in resolution, facilitating inspection of filopodial dynamics, growth cone migration and the outgrowth of thin neurites in the nerve ring that were otherwise obscured in either iSPIM or SDCM (Supplementary Videos 6,7 and Supplementary Fig. 12). We further focused our attention on neurite development in the AIY interneurons, which have been used to understand cell fate decisions, axon outgrowth and synaptogenesis during neuro-development[33-40] (Fig. 6a).

The adult AIY neurites have a very stereotypical morphology, with a portion of the neurite extending through the cord (termed zone 1), and a portion of the neurite extending dorsally through the nerve ring (termed zone 3) (Fig. 6b). The full pattern of AIY outgrowth has never been described, presumably because of difficulties in visualizing the small AIY process during axon extension in embryogenesis. We observed that the zone 3 region formed exclusively by axon outgrowth, whereas the zone 1 region formed as the AIY cell

body moved posteriorly in the animal, leaving behind an anchored extension (retrograde extension[41]; Fig. 6c and Supplementary Video 8).

Unlike iSPIM (Fig. 6c and Supplementary Video 7), diSPIM not only allowed us to visualize these processes qualitatively, but also enabled quantitative analysis of the outgrowth dynamics both pre- and post-twitching. We observed that AIY first extended a small projection, which grew at a rate of 0.2 μm/min (Fig. 6b, interval A). This projection developed into zone 3, which underwent outgrowth at a similar rate of 0.2 μm/min (Fig. 6b, interval B). Zone 1 development, by means of retrograde extension, began as zone 3 outgrowth finished, with zone 1 growth occurring at rates of 0.1–0.07 μm/min (Fig. 6b, interval C–D). Our findings indicate that retrograde extension can coexist with axon outgrowth to control neuromorphogenesis. Interestingly, zone 1 and zone 3 are also functionally distinct, as zone 3 contains all synapses in AIY, and zone 1 is an asynaptic region. Our results therefore suggest a link may exist between synaptic polarity and neurodevelopmental dynamics, underscoring the value of diSPIM for imaging neurodevelopment in 4D.

DISCUSSION

We acquired only two views while keeping the sample stationary, maximizing data acquisition speed while retaining the spatial resolution advantage provided by our joint deconvolution algorithm. Our algorithm may, however, also be used in other LSFM implementations, particularly those that obtain multiple specimen views by means of physical sample rotation. Although we did not investigate the effect of adding more views, we suspect that the signal-to-noise ratio would be improved at the cost of speed and additional illumination dose. Additional specimen views may also prove useful in reducing or compensating for the effects of scattered light or aberrations that plague any individual view. Combination of diSPIM with two-photon light sheet illumination may also help in reducing scattering and increasing depth penetration[42]. We note that spatial resolution would be improved if a higher detection NA objective were used, if more realistic (non-Gaussian) models of the PSF were employed or possibly if alternate (non-Richardson-Lucy) algorithms were used in our joint deconvolution method. Nevertheless, our current method offers improved performance in almost all areas when compared to other 4D imaging technologies.

Although SDCM has been the technique most commonly applied to 4D fluorescence imaging of live organisms[43], diSPIM offers better axial resolution (~2× improvement), ~10× faster volumetric acquisition rates and far less photobleaching (7.6-fold). Although the theoretical lateral resolution of SDCM is higher than our system, we found the greatly increased signal-to-noise ratio of our method usually provided higher lateral resolution in practice (e.g., in Fig. 3). Combining Bessel beam illumination with an improved structured illumination method offers marginally higher lateral resolution[31], but diSPIM offers equivalent (or better) axial resolution (~330 nm), 10–100× faster volumetric imaging rates (0.5–1 s instead of 10–100 s) and the ability to image over ~10× more time points (~1,000 instead of ~100), presumably due to the considerably lower illumination dose employed in our experiments and the lack of extraneous illumination outside the focal plane.

ONLINE METHODS

DiSPIM body

All optics and optomechanics were bolted onto a $4' \times 4'$ optical table (TMC, 784-647-02DR and 14-416-33) to minimize vibrations. A rapid automated modular microscope (Applied Scientific Instrumentation, RAMM) served as the base for diSPIM experiments. We designed a custom objective mount (Applied Scientific Instrumentation, RAO-DUAL-PI) that held the two diSPIM objectives in a perpendicular orientation and above the sample (Fig. 1). The objective mount was bolted onto an automated translation stage (Applied Scientific Instrumentation, LS50) for gross positioning of the SPIM objective mount above the sample before imaging, and the combined mount/stage was bolted onto the RAMM. The objective mount also housed piezoelectric objective positioners (Physik Instrumente, PIFOC-P726), enabling us to move each diSPIM detection objective in sync with the corresponding light sheet, to ensure coincidence between excitation and detection planes.

We also added an automated *xy* stage equipped with a *z* piezo (Applied Scientific Instrumentation, PZ-2000) to the RAMM base, for precisely positioning the sample at the focal/imaging plane of each objective before imaging. Rectangular coverslips containing the sample were placed in an autoclavable stainless steel rectangular chamber with removable bottom (Applied Scientific Instrumentation, I-3078-2450), and sealed in place with an O-ring (1.5 mm thickness, 40 mm inner diameter). This imaging chamber was placed into a stage insert (Applied Scientific Instrumentation, I-3078) and the insert mounted to the PZ-2000 stage. Worm embryos were screened initially using a 10×, 0.3 NA air objective (Olympus, 1-U2B524) mounted in the epi-fluorescence module of the RAMM (Applied Scientific Instrumentation, MIM-INVERTED-BASIC), using room lighting for illumination and an EM-CCD camera (Andor iXon DU-885) for detection. We note that neither PZ-2000 nor LS50 stages are moved during diSPIM acquisition, as the sample is not translated to acquire imaging volumes. The only components mentioned above that move during image acquisition are the two piezoelectric objective positioners.

DiSPIM excitation optics

The output beam from a 50-mW, 488-nm laser (Newport, PC14584) was directed through a half wave plate (Thorlabs, WPH05M-488) and acousto-optic tunable filter (AOTF, Quanta Tech, AOTFnC-400.650-TN) for power and shuttering control. The resulting beam was directed onto a galvanometric mirror (GALVO1, Thorlabs, GVSM001), whose surface was reimaged onto the sample plane by lens pairs L1 and L2 (Thorlabs, AC254-200-A-ML and AC254-50-A-ML, f = 200 mm and f = 50 mm); L3 and L4 (Thorlabs, AC254-200-A-ML and AC254-250-A-ML, f = 20 mm and f = 250 mm); and L5 and OBJ A (for SPIM A excitation; Thorlabs, AC-254-300-A and Nikon, MRD07420, f = 300 mm and f = 5 mm) or L6 and OBJ B (for SPIM B excitation; Thorlabs, AC-254-300-A and Nikon, MRD07420, f = 300 mm and f = 5 mm). After L5 or L6, the excitation beams were reflected to OBJ A or OBJ B via dichroic mirrors (Chroma, ZT405/488/561rpc). Each lens pair was placed in a 4f imaging configuration, such that the front focal plane of the lens in the preceding pair coincided with the back focal plane of the lens in the next pair, and lenses in each pair were separated by the sum of their focal lengths, resulting in a magnification of (50/200) ×

$(250/200) \times (5/300) = 5.21 \times 10^{-3}$ between GALVO1 and the sample plane, a beam waist of ~1.2 μm, a Rayleigh range of ~9 μm and a confocal parameter of ~18 μm.

Striping artifacts were minimized by scanning GALVO1 over an angular range of $\pm\ 0.02°$ (mechanical) at 2 KHz, as previously described[6]. A second galvanometric mirror (GALVO2, Thorlabs, GVSM001) was placed at the front focal plane of L1 and reimaged to the back focal planes of OBJ A and OBJ B via lens pairs L2/L3 and L4/L5 or L2/L3 and L4/L6. Scanning GALVO2 over an angular range of $\pm\ 0.95$ degrees (mechanical) translated the illumination laterally at the sample plane, defining a light sheet with lateral dimensions ~70 μm. A third galvanometric mirror (GALVO3, Thorlabs, GVSM001) was placed at the front focal plane of L3 (conjugate to GALVO2) and reimaged to the back focal planes of OBJ A and OBJ B via lens pair L4/L5 or L4/L6. Scanning GALVO3 over an angular range of $\pm\ 0.17$ degrees (mechanical) translated the light sheet axially at the sample plane, defining an excitation volume of ~50 μm thickness.

To provide equivalent illumination to both iSPIM arms, we placed a nonpolarizing beam-splitting cube (BS, Thorlabs, CM1-BS013) after L4. Independent, vibration-free shuttering in each illumination arm was achieved using liquid-crystal shutters (SHUTTER, Meadowlark Optics, LCS-200-0488/0561 and CellDrive3100) placed before L5 (for SPIM A shuttering) or L6 (for SPIM B shuttering).

For dual-color experiments, we coupled a 50-mW, 561-nm laser beam into the excitation path (Crystalaser, CL-561-050) by means of a dichroic mirror (DC, Semrock, Di01-R488-25x36), after first passing the beam through a half-wave plate (Thorlabs, WPH05M-532). These elements are shown in Supplementary Figure 1 in two perpendicular views.

DiSPIM detection optics

Fluorescence was collected via each 0.8 NA, 40× iSPIM detection objective, transmitted through dichroic mirrors (Chroma, ZT405/488/561rpc), filtered through long-pass and notch emission filters (Semrock, LP02-488RU-25 and NF03-561E-25) to reject 488-nm and 561-nm pump light, respectively, and imaged with 200-mm tube lenses (Applied Scientific Instrumentation, C60-TUBE_B) onto scientific-grade, complementary, metaloxide semiconductor (sCMOS) cameras (PCO, Edge), each operated at 200-Hz acquisition rate. The resulting image pixel size was 6.5 μm/40 = 162.5 nm.

DiSPIM data acquisition

Use of sCMOS cameras enables data acquisition with a unique combination of speed and low readout noise, but these devices require careful control for optimal operation. Our cameras provide two modes of operation: global shutter and rolling shutter. In global shutter mode, all rows are read out simultaneously, simplifying data acquisition and relaxing synchronization requirements between light sheet illumination and detection. Rolling shutter mode provides faster frame rates, fewer hot pixels and lower noise (Supplementary Fig. 7) than global shutter mode, but rows are read out sequentially. The sequential readout mode introduces temporal artifacts if illumination is not properly synchronized with acquisition (Supplementary Figs. 5 and 6). We operated our cameras in a hybrid rolling/global shutter

mode by illuminating the sample only when all lines were exposed, thus maintaining the benefits of rolling shutter mode while ensuring artifact-free imaging (Supplementary Fig. 8).

Two 16-bit DAQ cards (National Instruments, PCI 6733) were used in conjunction with custom software written in Labview (National Instruments) and the Python programming language to control dual-view iSPIM data acquisition. Acquisition included driving and synchronizing (i) the two electrooptic elements that provided shuttering in each view; (ii) the external trigger of each sCMOS camera, in order to implement hybrid global/rolling shutter mode; (iii) the anti-striping GALVO1; (iv) GALVO2 that laterally translated the excitation beam in order to define the light sheet; (v) GALVO3 that axially translated the excitation sheet, thus defining an excitation volume; (vi) the piezoelectric objective positioners that imaged each excitation plane and maintained focus; (vii) the AOTF that controlled power levels and hybrid global/rolling shutter mode.

The entire control scheme is illustrated in Supplementary Figure 6. As shown, two digital pulse trains produced by two DAQ counters were used for triggering the two sCMOS cameras. A simple digital circuit (AND Gate CD4081BE, Texas Instruments) was used to provide AND logic to the AOTF blanking input, switching the laser beam ON or OFF. The excitation power within a volume could be further modulated by the AOTF by driving a single-line input with an analog triangle waveform. Five other analog step-wise triangle waveforms were scaled appropriately (Stanford Research Systems, mainframe SIM900 and amplifier SIM983) and used to drive the three galvanometric mirrors (GALVO1, GALVO2 and GALVO3) and the two piezoelectric objective stages. All pulse trains and analog waveforms were synchronized with two digital pulses, which also controlled the optical shutters. Control software is available upon request from the authors.

In each 3D stack, 50 or 100 *xy* planes separated by a *z* step of 1 μm (Fig. 5) or 0.5 μm (Figs. 3,4 and 6) were imaged, resulting in a volume with dimensions 480 × 432 × 50 pixels or 480 × 432 × 100 (width × length × depth), corresponding to dimensions 78 μm × 70 μm × 50 μm. Each plane was acquired with exposure time 3 ms (total frame time ~5.1 ms), for a dual-view volumetric imaging time of 0.51 s (50 planes in each volume, or 100 planes per dual-view volume) or 1.02 s (100 planes in each volume, or 200 planes per dual-view volume), and spooled directly to a RAID disk (LSI MR9261-8i SCSI disk).

diSPIM excitation power and energy density

For 15 volumes/min experiments on cells (Figs. 3 and 4), we used the AOTF to adjust 488-nm excitation power (measured after lens L5 and L6, before diSPIM objectives) to 200 μW for the entire imaging period (~7 min). For 1 volume/min experiments on the BV24 GFP-histone line (Fig. 5), 488-nm excitation power was varied over imaging depth and time. For the first 90 min of measurement, power was held constant at 100 μW at all imaging depths. At later time points (2:40 h post fertilization to hatching), we linearly increased power through imaging depth to compensate for loss of signal due to scattering, from 60 μW at the surface to 120 μW at 40 μm depth. As 100 planes were collected for both views and the effective exposure time for each plane was 3 ms, the total energy delivered to the embryo during the 13 h imaging period was ~0.018 J (corresponding to an energy density of ~0.3 μJ/μm^3, considering a typical embryo size of ~50 μm × 40 μm × 30 μm). Assuming 780

dual-view volumes are measured in the entire imaging period, this implies an energy of ~23 μJ and energy density of 0.38 nJ/μm^3 per dual-view stack. For 3 volumes/min measurements on the DCR553 neuronal line (Fig. 6), we set the 488-nm excitation power to 100 μW over a 5-h imaging period. Thus the total energy and energy density delivered to the embryo was ~0.027 J and ~0.45 μJ/μm^3, respectively. As a total of ~900 dual-view volumes were collected, the energy and energy density for each dual-view stack were ~30 μJ and 0.5 nJ/μm^3, respectively.

Spinning disk confocal microscopy

For nematode studies, we used the same spinning disk confocal system (Quorum Technologies, Quorum Wave FX) as before[6]. *C. elegans* BV24 GFP-histone 4D confocal images were acquired with a 40× 1.3 NA PlanApo oil objective (Zeiss, 420762-9800-000) and an EM-CCD (Hamamatsu). Volumes were recorded at a temporal resolution of 1 min for embryos from 1:10 h.p.f. (hours post fertilization) to 7:20 h.p.f. or from 6:50 h.p.f. to 13:00 h.p.f. , with 30 planes per volume and an exposure time of 135 ms per plane, with a total energy and energy density of 0.018 J and 0.3 μJ/μm^3, respectively.

For cellular imaging, we used another SDCM system (Nikon TE-2000) equipped with a 60× 1.2 NA water objective. Cells were imaged every 12 s, obtaining 50 planes per volume with a spacing of 0.2 μm between planes. The total imaging time per plane was 240 ms, whereas the effective exposure time per plane was 100 ms. As a 488-nm excitation power of 600 μW was delivered to samples, the total energy in the 5-min imaging period was 0.075 J.

Semi-manual microtubule 3D tip tracking

Deconvolved volumetric data sets were loaded into Imaris 7.6. Voxel size was set to 162.5 nm/pixel in all three spatial dimensions, and the time between volumetric frames set to 4 s in accordance with experiment. Using the ImarisSurpass toolbox, a new spot was created for each track. The manual tracking option was selected along with the auto connect consecutive frames functionality. The user visually inspected the image sequence in order to find the brightest and clearest tracks. Then, the center of the microtubule tip was selected (the brightest pixel in the volume is located by ImarisSurpass) on a frame-by-frame basis from the starting point of the track until the track disappeared or ceased to be trackable. A minimum of 75 tracks were collected for each condition (i.e., thick cell on coverslip, thin cell on coverslip, thick cell in collagen gel) from either two or three cells (at least 25 tracks per cell). In the ImarisVantage toolbox, the *x/y/z* track displacements, mean track speeds and track durations were exported to an Excel spreadsheet, where a 45 degree rotation was implemented in order to rotate the reference frame into the coordinates displayed in Figures 3 and 4

$$
\begin{aligned}
x^{'} &= (x+z) \times \frac{\sqrt{2}}{2} \\
y^{'} &= y \\
z^{'} &= (x-z) \times \frac{\sqrt{2}}{2}
\end{aligned}
$$

The total track displacement was calculated as

$$L=\sqrt{(x'_{final}-x'_{initial})^2+(y'_{final}-y'_{initial})^2+(y'_{final}-y'_{initial})^2}$$

And the angle from the *z* axis as

$$\varphi=arccos\left(\frac{z'_{final}-z'_{initial}}{L}\right)\times\frac{180}{\pi}$$

Data processing

Registration, transformation, arithmetic fusion and joint deconvolution processing operations are employed sequentially to produce the dual-view volumetric data sets presented in Figures 2-6. The first three operations were implemented in the open-source MIPAV programming environment (http://mipav.cit.nih.gov/), and the latter in Python[44] and Matlab. Details follow (see also Supplementary Fig. 2).

Registration

An early time point in each 4D data series was selected to find the transformation matrix that was later used to register perpendicular volumes in subsequent time points. The volume corresponding to view$_B$ at this time point was rotated by 90 degrees to place views A and B in approximately the same orientation. We then applied an affine transform with 12 degrees of freedom (DOF) to optimize the registration of the rotated view$_B$ to the view$_A$. The DOF matrix is a direction cosine matrix that correlates the four affine image transformation operations (translation, rotation, scaling and skewing) from view$_B$ to view$_A$. We used an intensity-based method extended from Wood[44] to iteratively vary the DOF matrix and apply it to the rotated view$_B$. To optimize DOF values, a correlation ratio cost function was minimized using Powell's method (http://math.fullerton.edu/mathews/n2003/PowellMethodMod.html). The final result of this process is the 12-element DOF transformation matrix. Obtaining the transformation matrix takes ~10 min on a 64-bit Windows, 2.4 GHz/6-core/12-thread processor with 6 GB RAM. This registration function 'Optimized Automatic Image Registration 3D' has already been incorporated in MIPAV and its source code is available in the file 'gov.nih.mipav. model.algorithms.registration.AlgorithmRegOAR3D.java'.

Transformation

This transformation matrix is applied to transform all subsequent view$_B$ volumes in the time series into proper registration with view$_A$ volumes. We typically set up multiple parallel transform operations using the 6-core machine described above. All raw volumes were acquired at significantly larger axial pixel size (i.e., 0.5 μm or 1 μm) than lateral pixel size (0.1625 μm). Trilinear interpolatio[45] was applied to upsample the pixel grid in both transformed B and raw view$_A$ volumes, resulting in isotropic pixels with 0.1625 μm dimensions.

Arithmetic fusion

Background intensity and partial voluming effects may exist in both the transformed B and the view$_A$ volumes as a result of the acquisition process. Partial voluming may also occur after registration has been performed. Partial voluming refers to the inclusion, within a single pixel, of both the cell of interest and background intensity values. This usually produces a pixel value that is lower than if the pixel had contained only the cells of interest. To isolate those pixels that entirely contain the cells of interest, these low-intensity effects can be removed by specifying an upper-bound pixel value, below which all pixels with intensity values between 0 and this upper bound are thresholded to zero. After this optional thresholding step, transformed view$_B$ and view$_A$ volumes were combined using an equally weighted arithmetic mean. This arithmetic fusion was only used in Figure 2 and as the initial estimate in the deconvolution process. A new MIPAV plugin 'SPIM' has been developed to parallelize both the transformation and fusion operations, and is available upon request. It takes ~2 h to process 1,000 time points with a 6-core machine equipped with a MegaRAID device (LSI MR9261-8i SCSI disk).

Deconvolution

The Richardson-Lucy iterative deconvolution algorithm, which provides maximum-likelihood estimation when the signal displays Poisson statistics, has been commonly used to improve resolution, signal and contrast in fluorescence images. Here we design a modification of the algorithm to deal with the transformed view$_B$ and the view$_A$ volumes. Each iteration involves two steps

$$
\begin{aligned}
Estimate_{k+1} &= Estimate_k \times Blur_A \left(\frac{View_A}{Blur_A(Estimate_k)} \right) \\
Estimate_{k+2} &= Estimate_{k+1} \times Blur_B \left(\frac{View_B}{Blur_B(Estimate_{k+1})} \right)
\end{aligned}
$$

where view$_A$ is the upsampled (i.e., coarsely sampled axial pixels were linearly interpolated to obtain an isotropic voxel size of $0.1625 \times 0.1625 \times 0.1625 \ \mu m^3$) A volume, blur$_A$ corresponds to convolution with the PSF associated with the view$_A$, view$_B$ is the transformed B volume and blur$_B$ corresponds to convolution with the PSF associated with the transformed viewB. With an initial estimate Estimate$_0$ provided by the arithmetic fusion of the dual view data as mentioned above, ~10 iterations provide most of the improvement, whereas convergence is reached in ~30 iterations (Supplementary Fig. 3).

All deconvolutions that we performed employed simple 3D Gaussian blurring functions, with parameters based on the measurements from 10 100-nm yellow-green fluorescent beads (Supplementary Table 1; $\sigma_{lateral} = 0.20 \ \mu m$, $\sigma_{axial} = 0.62 \ \mu m$ for view$_A$; $\sigma_{lateral} = 0.19 \ \mu m$, $\sigma_{axial} = 0.66 \ \mu m$ for view$_B$). Compared to the direct use of measured PSFs, the benefits of using a model function include less noise amplification and the computational advantage of separable convolution along each axis. Use of the Gaussian PSF greatly improved the raw resolution present in single view iSPIM and approached the theoretical resolution predicted by our 0.8 NA lens. We suspect that more accurate results may be obtained if blind deconvolution, measured PSFs taken at very high signal-to-noise ratio or spatially varying PSFs are used, but we did not use any of these methods in this paper.

This joint deconvolution method has been implemented in both Python and Matlab (available upon request). With a single core, joint deconvolution of one dual-view volume takes ~100 seconds; processing 1,000 dual-view volumes finishes in ~5 h with multiple parallel jobs on a 6-core machine.

Worm strains

Worms were raised under standard conditions at 20oC on NGM media seeded with E. coli OP50. Strain BV24 ([ltIs44 [pie-1p-mCherry: :PH(PLC1delta1) + unc-119(+)]; zuIs178 [(his-72 1kb : : HIS-72 : : GFP); unc-119(+)] V]) was used to image nuclei. zuIS178 is an integrated transgene which expresses a ubiquitously expressed histone-GFP fusion throughout embryogenesis. ltIS44 is an integrated transgene which expresses membrane-localized mCherry, which is not used in imaging.

Strain DCR553 (mgIS18 IV pttx-3b: :GFP; lqIS4 X pceh-10: :GPF) was used to image neurons. mgIS18 is an integrated transgene labeling a subset of neurons, including AIY, with GFP during embryonic development (GFP expression is restricted to AIY neurons in post-hatching larval and adult animals). lqIS4 is an integrated transgene labeling an additional subset of neurons with GFP during embryonic and post-embryonic development; the only neuron with shared expression between the two promoters is AIY. Combinatorial expression with these two promoters is used to provide consistent GFP labeling of AIY in worm embryo throughout embryonic development. Worm embryos were prepared for diSPIM imaging as previously described[6].

Cell culture and collagen gel preparation

Human umbilical vein cells were maintained in complete Endothelial Growth Medium (EGM; Lonza). Cells were transfected with plasmids encoding GFP- or tdTomato-EB3 via electroporation (Lonza) 12–18 h prior to imaging, and replated onto coated glass coverslips or into collagen gels 1–4 h prior to imaging. For imaging cells adherent to glass, coverslips were coated with 100 μg/ml native collagen I neutralized with 10× MEM media (diluted with collagen solution to 1×), with addition of $NaHCO_3$. Coverslips were coated for >4 h at 37 °C in a humidified chamber, then rinsed several times with 1× phosphate buffered saline (PBS). Cells were seeded on coverslips in EGM supplemented with 30 mM HEPES, pH 7.5, (imaging medium) and allowed to adhere for 1-2 h prior to imaging.

Preparation of and culturing of cells within collagen gels was performed essentially as described previously[46,47]. Native collagen I was diluted to 2 mg/ml in a solution with 10× MEM diluted to 1× and neutralized with $NaHCO_3$. Collagen gel solutions were spread in small (20–50 μl) amounts to form a 20–40 μm thick gel (previously determined by collagen fiber reflectance), and allowed to polymerize onto cleaned glass coverslips for 1 h at 37 °C in a humidified chamber. Cells were seeded onto the gels in a small amount of media and allowed to adhere for 1 h, and an additional small amount of gel was added on top and allowed to polymerize for an additional hour. Gels were maintained in imaging medium and imaged as described.

Supplementary Material

Refer to Web version on PubMed Central for supplementary material.

References

1. Voie AH, Burns DH, Spelman FA. Orthogonal-plane fluorescence optical sectioning: three-dimensional imaging of macroscopic biological specimens. J Microsc. 1993; 170:229–236. [PubMed: 8371260]

2. Fuchs E, Jaffe JS, Long RA, Azam F. Thin laser light sheet microscope for microbial oceanography. Opt Express. 2002; 10:145–154. [PubMed: 19424342]

3. Huisken J, Swoger J, Del Bene F, Wittbrodt J, Stelzer EHK. Optical sectioning deep inside live embryos by selective plane illumination microscopy. Science. 2004; 305:1007–1009. [PubMed: 15310904]

4. Holekamp TF, Turaga D, Holy TE. Fast three-dimensional fluorescence imaging of activity in neural populations by objective-coupled planar illumination microscopy. Neuron. 2008; 57:661–672. [PubMed: 18341987]

5. Huisken J, Stainier DY. Selective plane illumination microscopy techniques in developmental biology. Development. 2009; 136:1963–1975. [PubMed: 19465594]

6. Wu Y, et al. Inverted selective plane illumination microscopy (iSPIM) enables coupled cell identity lineaging and neurodevelopmental imaging in *Caenorhabditis elegans*. Proc Natl Acad Sci USA. 2011; 108:17708–17713. [PubMed: 22006307]

7. Capoulade J, Wachsmuth M, Hufnagel L, Knop M. Quantitative fluorescence imaging of protein diffusion and interaction in living cells. Nat Biotechnol. 2011; 29:835–839. [PubMed: 21822256]

8. Fahrbach FO, Simon P, Rohrbach A. Microscopy with self-reconstructing beams. Nat Photonics. 2010; 4:780–785.

9. Planchon TA, et al. Rapid three-dimensional isotropic imaging of living cells using Bessel beam plane illumination. Nat Methods. 2011; 8:417–423. [PubMed: 21378978]

10. Swoger J, Verveer P, Greger K, Huisken J, Stelzer EHK. Multi-view image fusion improves resolution in three-dimensional microscopy. Opt Express. 2007; 15:8029–8042. [PubMed: 19547131]

11. Temerinac-Ott M, et al. Multiview deblurring for 3-D images from light-sheet-based fluorescence microscopy. IEEE Trans Image Process. 2012; 21:1863–1873. [PubMed: 22203719]

12. Verveer PJ, et al. High-resolution three-dimensional imaging of large specimens with light sheet-based microscopy. Nat Methods. 2007; 4:311–313. [PubMed: 17339847]

13. Tomer R, Khairy K, Amat F, Keller PJ. Quantitative high-speed imaging of entire developing embryos with simultaneous multiview light-sheet microscopy. Nat Methods. 2012; 9:755–763. [PubMed: 22660741]

14. Krzic U, Gunther S, Saunders TE, Streichan SJ, Hufnagel L. Multiview light-sheet microscope for rapid in toto imaging. Nat Methods. 2012; 9:730–733. [PubMed: 22660739]

15. Swoger J, Huisken J, Stelzer EHK. Multiple imaging axis microscopy improves resolution for thick-sample applications. Opt Lett. 2003; 28:1654–1656. [PubMed: 13677526]

16. Schmid B, et al. High-speed panoramic light-sheet microscopy reveals global endodermal cell dynamics. Nat Commun. 2013; 4:2207. [PubMed: 23884240]

17. Richardson WH. Bayesian-based iterative method of image restoration. J Opt Sci Am. 1972; 62:55–59.

18. Lucy LB. An iterative technique for the rectification of observed distributions. Astron J. 1974; 79:745–754.

19. Dey N, et al. Richardson-Lucy algorithm with total variation regularization for 3D confocal microscope deconvolution. Microsc Res Tech. 2006; 69:260–266. [PubMed: 16586486]

20. Krzic, U. PhD thesis. University Heidelberg; 2009. Multiple-view Microscopy with Light-Sheet Based Fluorescence Microscope.

21. Desai A, Mitchison TJ. Microtubule polymerization dynamics. Annu Rev Cell Dev Biol. 1997; 13:83–117. [PubMed: 9442869]

22. Akhmanova A, Hoogenraad CC. Microtubule plus-end tracking proteins: mechanisms and functions. Curr Opin Cell Biol. 2005; 17:47–54. [PubMed: 15661518]

23. Matov A, et al. Analysis of microtubule dynamic instability using a plus-end growth marker. Nat Methods. 2010; 7:761–768. [PubMed: 20729842]

24. Dogterom M, Yurke B. Measurement of the force-velocity relation for growing microtubules. Science. 1997; 278:856–860. [PubMed: 9346483]

25. Kandere-Grzybowska K, Campbell C, Komarova Y, Grzybowski BA, Borisy GG. Molecular dynamics imaging in micropatterned living cells. Nat Methods. 2005; 2:739–741. [PubMed: 16179919]

26. Sulston JE, Schierenberg E, White JG, Thomson JN. The embryonic cell lineage of the nematode *Caenorhabditis elegans*. Dev Biol. 1983; 100:64–119. [PubMed: 6684600]

27. York AG, et al. Resolution doubling in live, multicellular organisms via multifocal structured illumination microscopy. Nat Methods. 2012; 9:749–754. [PubMed: 22581372]

28. Bao Z, et al. Automated cell lineage tracing in *Caenorhabditis elegans*. Proc Natl Acad Sci USA. 2006; 103:2707–2712. [PubMed: 16477039]

29. Santella A, Du Z, Nowotschin S, Hadjantonakis A-K, Bao Z. A hybrid blobslice model for accurate and efficient detection of fluorescence labeled nuclei in 3D. BMC Bioinformatics. 2010; 11:580. [PubMed: 21114815]

30. Giurumescu CA, et al. Quantitative semi-automated analysis of morphogenesis with single-cell resolution in complex embryos. Development. 2012; 139:4271–4279. [PubMed: 23052905]

31. Gao L, et al. Noninvasive imaging beyond the diffraction limit of 3D dynamics in thickly fluorescent specimens. Cell. 2012; 151:1370–1385. [PubMed: 23217717]

32. White JG, Southgate E, Thomson JN, Brenner S. The structure of the nervous system of the nematode *Caenorhabditis elegans*. Phil Trans R Soc Lond B. 1986; 314:1–340. [PubMed: 22462104]

33. Bhattacharya R, Townley RA, Berry KL, Bulow HE. The PAPS transporter PST-1 is required for heparan sulfation and is essential for viability and neural development in *C. elegans*. J Cell Sci. 2009; 122:4492–4504. [PubMed: 19920077]

34. Hobert O, et al. Regulation of interneuron function in the *C. elegans* thermoregulatory pathway by the ttx-3 LIM homeobox gene. Neuron. 1997; 19:345–357. [PubMed: 9292724]

35. Altun-Gultekin Z, et al. A regulatory cascade of three homeobox genes, ceh-10, ttx-3 and ceh-23, controls cell fate specification of a defined interneuron class in *C. elegans*. Development. 2001; 128:1951–1969. [PubMed: 11493519]

36. Wenick AS, Hobert O. Genomic cis-regulatory architecture and trans-acting regulators of a single interneuron-specific gene battery in *C. elegans*. Dev Cell. 2004; 6:757–770. [PubMed: 15177025]

37. Bulow HE, Berry KL, Topper LH, Peles E, Hobert O. Heparan sulfate proteoglycan-dependent induction of axon branching and axon misrouting by the Kallmann syndrome gene kal-1. Proc Natl Acad Sci USA. 2002; 99:6346–6351. [PubMed: 11983919]

38. Bertrand V, Hobert O. Linking asymmetric cell division to the terminal differentiation program of postmitotic neurons in *C. elegans*. Dev Cell. 2009; 16:563–575. [PubMed: 19386265]

39. Stavoe AK, et al. Synaptic vesicle clustering requires a distinct MIG-10/Lamellipodin isoform and ABI-1 downstream from Netrin. Genes Dev. 2012; 26:2206–2221. [PubMed: 23028145]

40. Colón-Ramos DA, Margeta MA, Shen K. Glia promote local synaptogenesis through UNC-6 (netrin) signaling in *C. elegans*. Science. 2007; 318:103–106. [PubMed: 17916735]

41. Heiman M, Shaham S. DEX-1 and DYF-7 establish sensory dendrite length by anchoring dendritic tips during cell migration. Cell. 2009; 137:344–355. [PubMed: 19344940]

42. Truong TV, Supatto W, Koos DS, Choi JM, Fraser SE. Deep and fast live imaging with two-photon scanned light-sheet microscopy. Nat Methods. 2011; 8:757–760. [PubMed: 21765409]

43. Fischer RS, Wu Y, Kanchanawong P, Shroff H, Waterman CM. Microscopy in 3D: a biologist's toolbox. Trends Cell Biol. 2011; 21:682–691. [PubMed: 22047760]

44. Woods, RP. Handbook of Medical Imaging Processing and Analysis. Bankman, Isaac N., editor. Academic Press; 2000. p. 529-553.

45. Lehmann TM, Gonner C, Spitzer K. Survey: interpolation methods in medical image processing. IEEE Trans Med Imaging. 1999; 18:1049–1075. [PubMed: 10661324]

46. Fischer RS, Myers KA, Gardel ML, Waterman CM. Stiffness-controlled three-dimensional extracellular matrices for high-resolution imaging of cell behavior. Nat Protoc. 2012; 7:2056–2066. [PubMed: 23099487]

47. Fischer RS, Gardel ML, Ma X, Adelstein RS, Waterman CM. Local cortical tension by myosin II guides 3D endothelial branching. Curr Biol. 2009; 19:260–265. [PubMed: 19185493]
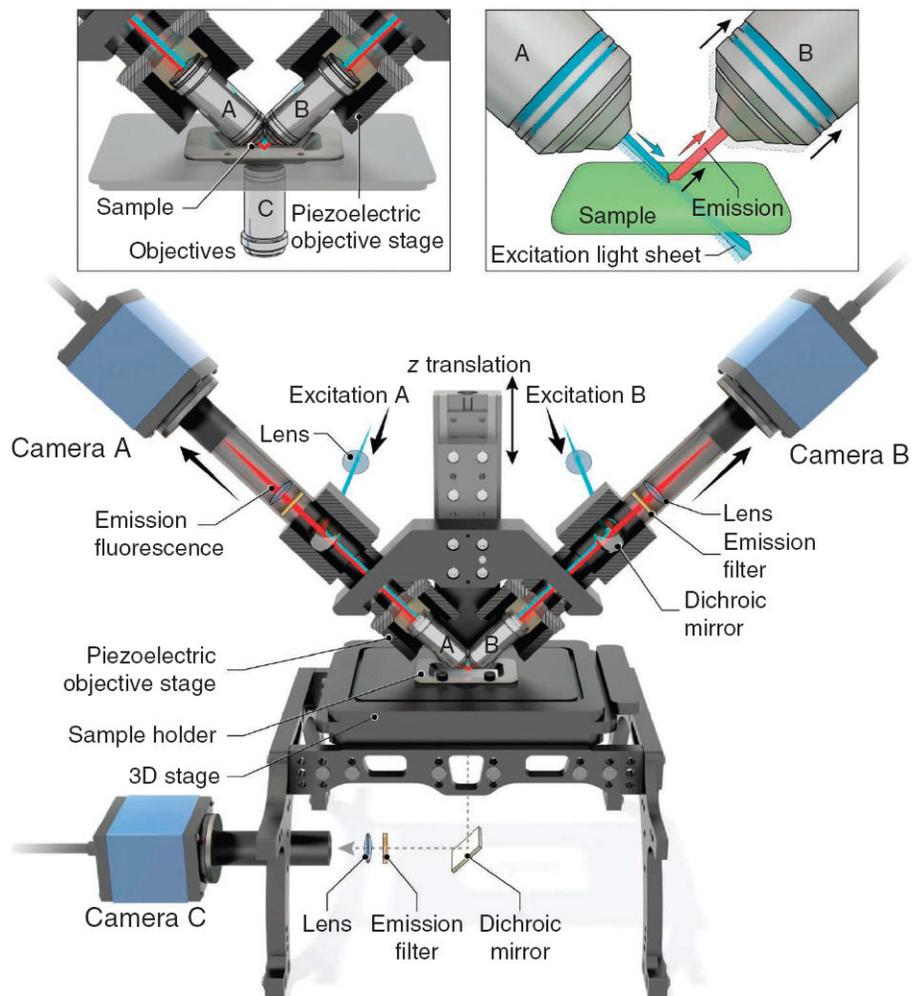
Figure 1.
Dual-view iSPIM setup. 0.8 NA water-immersion objectives (A/B) are mounted orthogonally onto a *z* translation stage that is bolted directly onto the illumination pillar of an inverted microscope. In conjunction with other optics (Supplementary Fig. 1), both objectives produce a light sheet at the sample. Excitation A(B) occurs via objective A(B), and the resulting fluorescence is collected through perpendicular objective B(A), and imaged onto camera B(A) by means of dichroic mirrors, emission filters and lenses. Excitation (blue) and detection (red) are shown occurring simultaneously along both light paths in the lower schematic, but in reality volumetric imaging occurs sequentially as shown in the upper right inset. During acquisition, sample and objective A(B) are held stationary, the light sheet is scanned through the sample using galvanometric mirrors (not shown), and a piezoelectric objective stage moves objective B(A) in sync with the light sheet, ensuring that excitation and/or detection planes are coincident. The sample is mounted onto a rectangular coverslip that is placed onto a 3D translation stage, ensuring correct placement relative to objectives. The sample may also be viewed through objective C (see upper left inset), dichroic mirror, emission filter, lens and camera C placed in the conventional light path of

the inverted microscope. This objective is particularly useful in finding or screening samples.
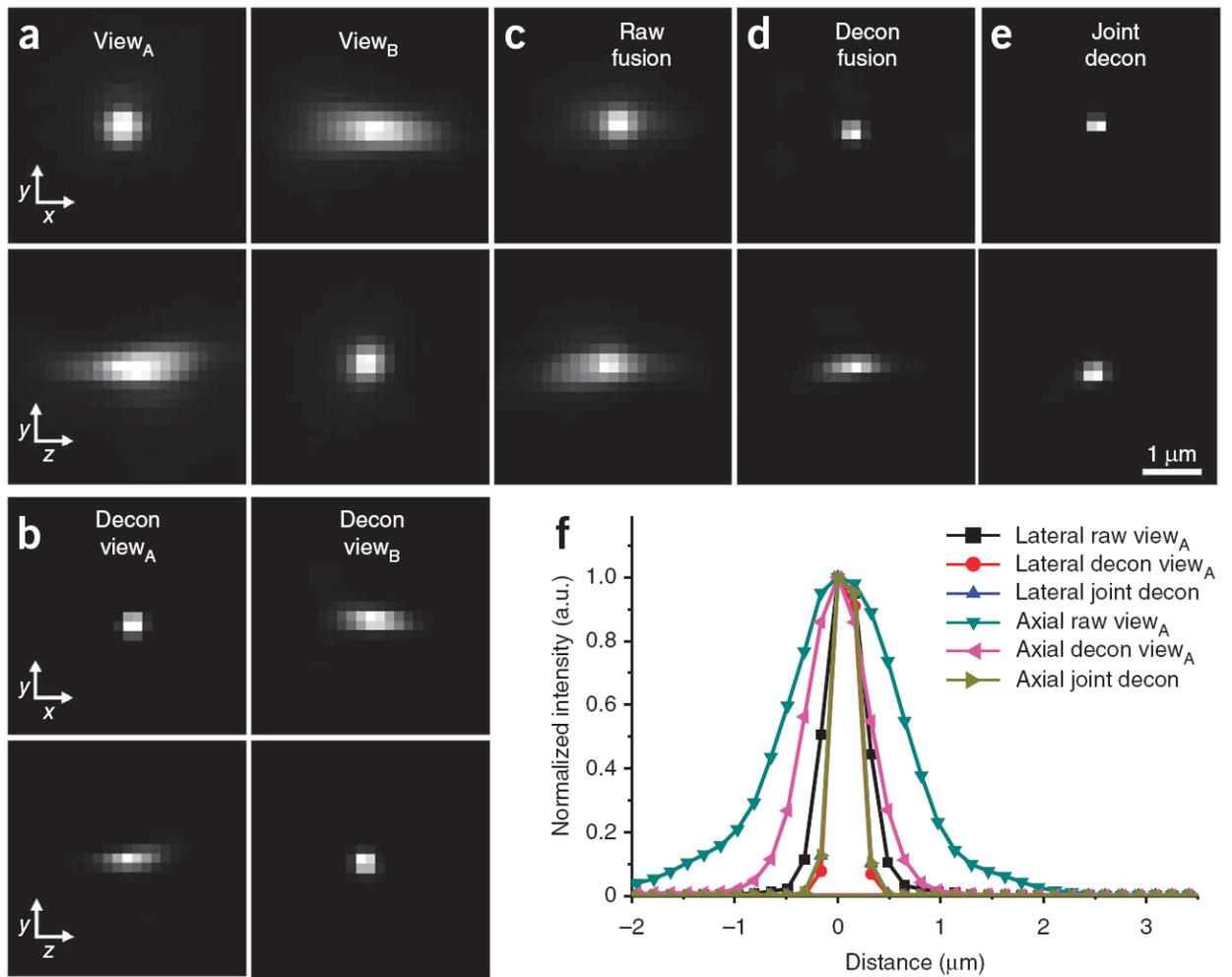
Figure 2.
Improving resolution isotropy with different fusion schemes. (**a–e**) Image planes from the center of volumetric data sets of 100-nm fluorescent beads, for single views (**a**), deconvolved single views (**b**), arithmetic fusion (**c**), deconvolved arithmetic fusion (**d**) and joint deconvolution (**e**). (**f**) Comparison of axial and lateral line profiles from (**a,b,e**). See also Supplementary Table 1 and Supplementary Video 1. *xy*: lateral view; *zy*; axial view.
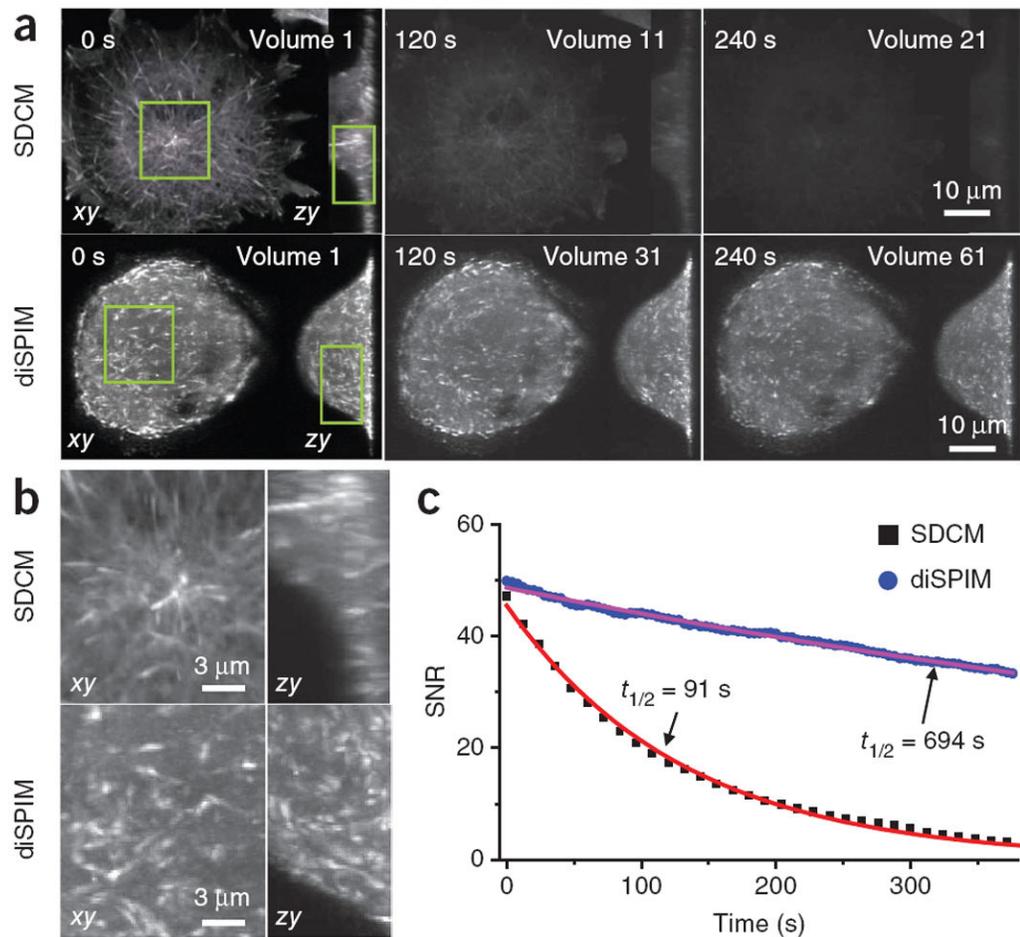
Figure 3.
Bleaching comparison between SDCM and diSPIM. (**a**) GFP-EB3 cells were imaged with SDCM (top row) and diSPIM (bottom row), at equivalent illumination dose. Cells imaged with SDCM were temporally sampled 3× less frequently than diSPIM (3× fewer total volumes, also 3.2× fewer planes per volume), but exhibited significantly more bleaching. (**b**) Higher magnification views of the green rectangular subregions in **a**. (**c**) The bleaching rate was quantified from a $20 \times 20 \ \mu m^2$ area inside each cell; signal-to-noise ratio (SNR) was calculated as the ratio of the averaged intensity of this area over the s.d. of the background in an identical area outside the cell. Data were fitted to single exponentials; half-time to complete bleaching is indicated on the graph. See also Supplementary Video 2.
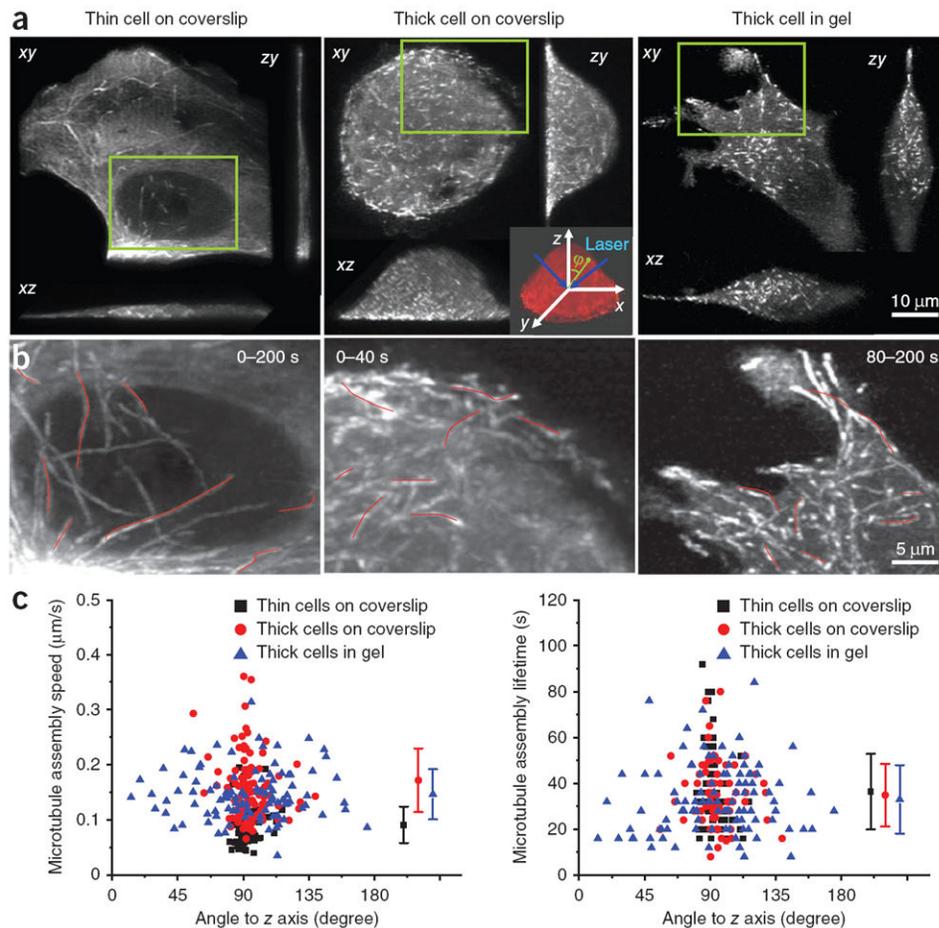
Figure 4.
Dual-view iSPIM enables microtubule tracking in 4D. (**a**) *xy, zy* and *xz* maximum-intensity projections from a single time point taken from a 5-min volumetric series, showing GFP-EB3–labeled microtubules in human umbilical vein cells, on coverslips (a thin cell, left column, and a thicker cell, middle) and inside a collagen gel (right). Inset indicates geometry of figure axes relative to the light sheet propagation axes. See also Supplementary Video 3. (**b**) Higher magnification views of the green rectangular subregions in **a**, projected over the indicated time interval and showing example tracks in red. (**c**) Quantification of average speed (left graph) and lifetime (right graph) as a function of angle relative to coverslip for the different samples. Mean and s.d. are shown for $N = 75$, 75 and 100 tracked tips (from three thin cells on coverslips, two thick cells on coverslips and three cells in gels) on the right-hand portion of each graph.
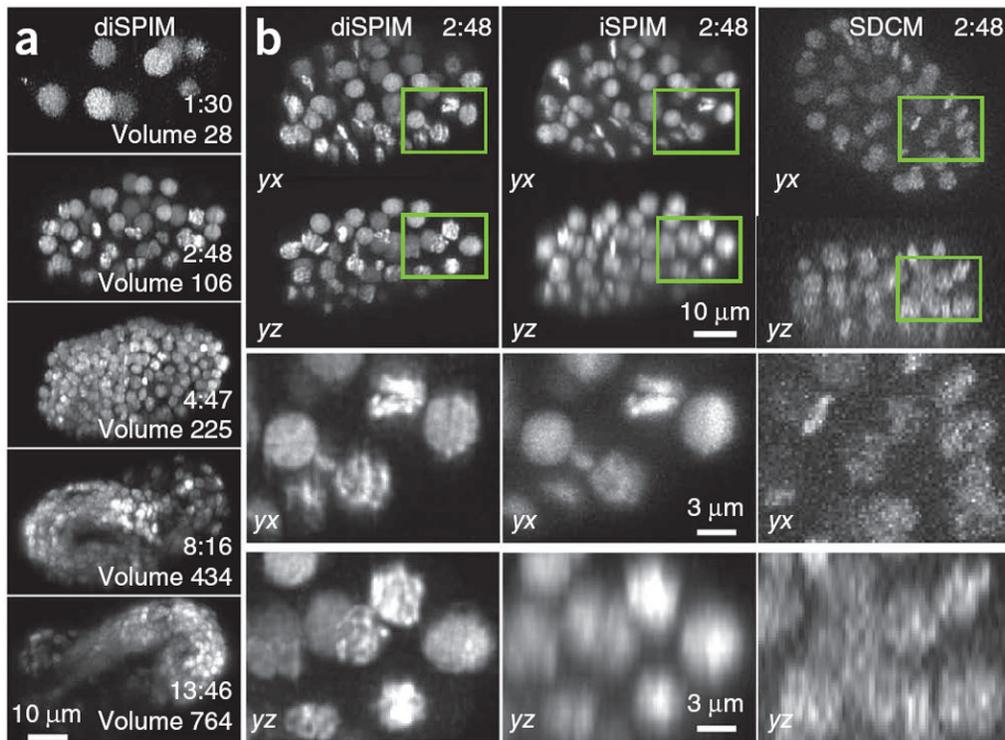
Figure 5.
Dual-view iSPIM improves axial resolution in 4D embryonic imaging. (**a**) Selected diSPIM maximum-intensity projections of GFP-labeled histones in nematode embryo, from 786 time-point volumetric series. Projections were computed 60 degrees relative to *y* axis. (**b**) Comparison between diSPIM (left column), single view iSPIM (middle) and SDCM (right) at the same time point in embryogenesis. Lower two rows: higher magnification views of boxed nuclei in top two rows. All times are hours:minutes post fertilization. Projections are taken at 0 or 90 degrees relative to *y* axis. See also Supplementary Videos 4,5 and Supplementary Figure 11.
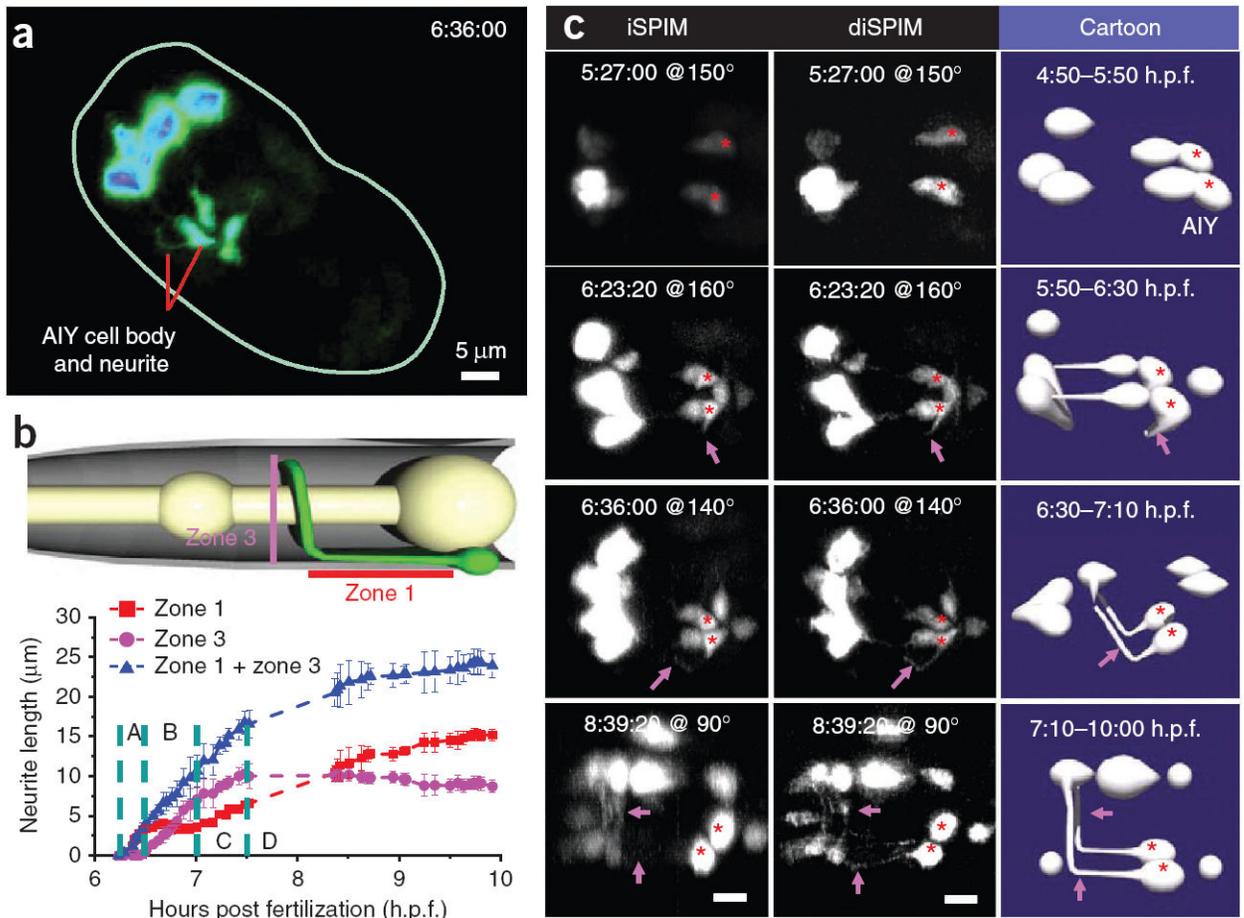
Figure 6.
Spatiotemporal dissection of AIY neurite outgrowth. (**a**) AIY neurons in the context of the developing nematode embryo. Outline indicates eggshell. (**b**) Top: AIY morphology in the adult nematode embryo, with zone 1 and zone 3 regions marked. Bottom: length of zones 1 and 3 during AIY development. Time intervals A–D are introduced to clarify description in text. The blank region (dashed lines in interval D) arises due to lowered expression of GFP during this period, probably due to the characteristics of the promoter region used. Data: mean ± s.d., from four embryos. (**c**) Maximum intensity projections from iSPIM (left column) and diSPIM (middle) at indicated times (and rotation angle relative to *y* axis). Volumes are taken from a 910 time-point series obtained from a single animal. Note the increased resolution of diSPIM better resolves fine neurites and cell bodies as compared to iSPIM. Red stars and pink arrows indicate the position of the AIY cell bodies and neurites, respectively. Right column: accompanying cartoon. Scale bars, 5 μm. All times are hours: minutes:seconds post fertilization. See also Supplementary Videos 7 and 8.